

FaceVR: Real-Time Facial Reenactment and Eye Gaze Control in Virtual Reality

Justus Thies¹ Michael Zollhöfer² Marc Stamminger¹ Christian Theobalt² Matthias Nießner³
¹University of Erlangen-Nuremberg ²Max-Planck-Institute for Informatics ³Stanford University

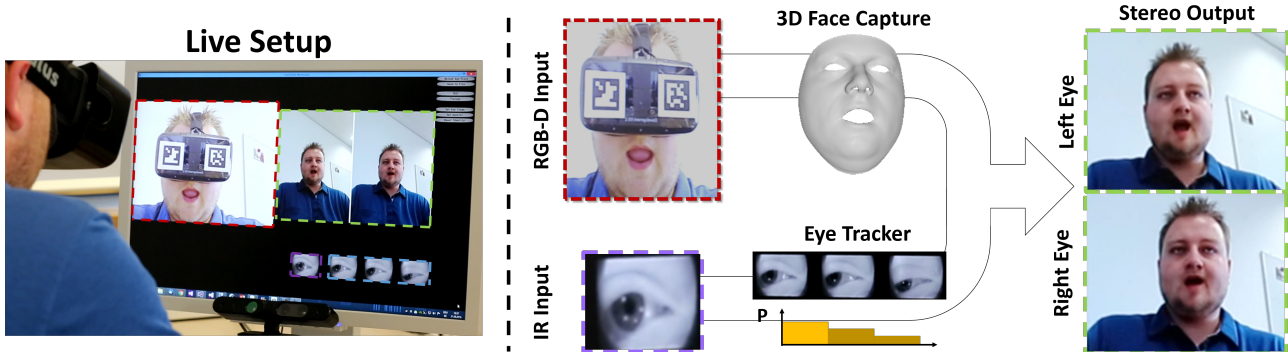


Figure 1: We present FaceVR, a novel method to perform real-time gaze-aware facial reenactment with a virtual reality device (left). In order to capture a face, we use a commodity RGB-D sensor with a frontal view; the eye region is tracked using a new data-driven approach based on data from an IR camera located inside the head-mounted display. Using the 3D reconstructed face as an intermediate, we can modify and edit the face, as well as re-render it in a photo-realistic fashion, allowing for a variety of applications; e.g., removal of VR goggles or gaze re-targeting. In addition, we render our output in stereo (right), which enables display on stereo devices such as other VR headsets.

Abstract

We introduce *FaceVR*, a novel method for gaze-aware facial reenactment in the Virtual Reality (VR) context. The key component of FaceVR is a robust algorithm to perform real-time facial motion capture of an actor who is wearing a head-mounted display (HMD), as well as a new data-driven approach for eye tracking from monocular videos. In addition to these face reconstruction components, FaceVR incorporates photo-realistic re-rendering in real time, thus allowing artificial modifications of face and eye appearances. For instance, we can alter facial expressions, change gaze directions, or remove the VR goggles in realistic re-renderings. In a live setup with a source and a target actor, we apply these newly-introduced algorithmic components. We assume that the source actor is wearing a VR device, and we capture his facial expressions and eye movement in real-time. For the target video, we mimic a similar tracking process; however, we use the source input to drive the animations of the target video, thus enabling gaze-aware facial reenactment. To render the modified target video on a stereo display, we augment our capture and reconstruction process with stereo data. In the end, FaceVR produces compelling results for a variety of applications, such as gaze-aware facial reenactment, reenactment in virtual reality, removal of VR goggles, and re-targeting of somebody’s gaze direction in a video conferencing call.

1 Introduction

Modern head-mounted virtual reality displays, such as the Oculus Rift™ or the HTC Vive™, are able to provide very believable and highly immersive stereo renderings of virtual environments to a user. In particular, for teleconferencing scenarios, where two or more people at distant locations meet (virtually) face-to-face in a virtual meeting room, VR displays can provide a far more immersive and connected atmosphere than today’s teleconferencing systems. Today’s commercial teleconferencing systems usually employ one or several video cameras at each end to film the participants, whose video(s) are then shown on one or several standard displays at the other end. Imagine one could take this to the next level, and two people in a VR teleconference would each see a photo-realistic 3D

rendering of their actual conversational partner, not simply an avatar, but in their own HMD. The biggest obstacle in making this a reality is that while the HMD allows for very immersive rendering, it is a large physical device which occludes the majority of the face. In other words, even if each participant of a teleconference was recorded with a 3D video rig, whose feed is streamed to the other end’s HMD, natural conversation is not possible due to the display occluding most of the face.

Recent advancements in VR displays are flanked by great progress in face performance capture methods. State-of-the-art approaches enable dense reconstruction of dynamic face geometry in real-time, from RGB-D [Weise et al. 2011; Bouaziz et al. 2013; Li et al. 2013; Zollhöfer et al. 2014; Hsieh et al. 2015] or even RGB cameras [Cao et al. 2014a; Cao et al. 2015; Thies et al. 2016]. A further step has been taken by recent RGB-D [Thies et al. 2015] or RGB-only [Thies et al. 2016] real-time facial reenactment methods. These methods estimate dense face geometry along with scene illumination of a source and target actor, transfer the source expression to the target, and re-render and composite the modified face and the target video in a photo-realistic fashion. In order to render the modified mouth in the target view, 3D shape proxies [Thies et al. 2015] or image-based methods [Thies et al. 2016] are used.

In the aforementioned VR teleconferencing setting, a (self-)facial reenactment approach could be used to remove the display from the face of each participant by rendering the unoccluded view of the face on top of the VR display at the other end. Unfortunately, the stability of many real-time face capture methods suffer if the tracked person wears an HMD. Furthermore, existing reenactment approaches cannot transfer the appearance of eyes, including blinking and eye gaze - yet exact reproduction of the entire face expression, including the eye region, is crucial for conversations in VR.

In our work, we therefore propose *FaceVR*, a new real-time facial reenactment approach that can transfer facial expressions and realistic eye appearance between a source and a target actor video. It is also suited for self-reenactment with HMDs, thus enabling VR teleconferencing as described above. In order to achieve this goal, we make several algorithmic key contributions:

- Robust real-time facial performance capture of a person wearing an HMD, using an outside-in RGB-D camera stream with rigid and non-rigid degrees of freedom.
- Real-time eye-gaze tracking with a novel classification approach based on random ferns, both within an HMD and from an external camera.
- Facial reenactment with photo-realistic re-rendering of the face region including the mouth and the eyes, using model-based face, appearance, and lighting capture.
- Capture of target actors using a lightweight stereo rig which significantly improves tracking accuracy over monocular setups and enables photo-realistic re-rendering of stereo content.
- An end-to-end system for facial reenactment in VR, where the source actor is wearing an HMD and the target actor is recorded in stereo. This facilitates VR goggle removal from a video stream, allows for gaze-aware VR conversations, and enables many other reenactment applications such as eye-gaze correction in video chats.

2 Related Work

A variety of methods exist to capture detailed static and dynamic face geometry with specialized controlled acquisition setups [Klehm et al. 2015]. Some methods use passive multi-view reconstruction in a studio setup [Borshukov et al. 2003; Pighin and Lewis 2006; Beeler et al. 2011; Fyffe et al. 2014], optionally with the support of invisible makeup [Williams 1990] or face markers [Huang et al. 2011]. Methods using active scanners for capture were also developed [Zhang et al. 2004; Weise et al. 2009].

Many approaches employ a parametric model of face identity [Blanz and Vetter 1999; Blanz et al. 2003], and face expression [Tena et al. 2011]. Blend shape models are widely used for representing the expression space [Pighin et al. 1998; Lewis et al. 2014], and multi-linear models jointly represent the identity and expression space [Vlasic et al. 2005; Shi et al. 2014]. Newer methods enable dense face performance capture in more general scenes with more lightweight setups, such as a stereo camera [Valgaerts et al. 2012], or even just a single RGB video at off-line frame rates [Garrido et al. 2013; Suwajanakorn et al. 2014; Shi et al. 2014; Fyffe et al. 2014]. Garrido et al. [2016] reconstruct a fully controllable parametric face rig including reflectance and fine scale detail, and [Suwajanakorn et al. 2015] build a modifiable mesh model of the face. [Ichim et al. 2015] reconstruct a game-type 3D face avatar from static multi-view images and a video sequence of face expressions. More recently, methods reconstructing dense dynamic face geometry in real-time from a single RGB-D camera [Weise et al. 2011; Zollhöfer et al. 2014; Bouaziz et al. 2013; Li et al. 2013; Hsieh et al. 2015] were proposed. Some of them estimate appearance and illumination along with geometry [Thies et al. 2015]. Using trained regressors [Cao et al. 2014a; Cao et al. 2015], or parametric face models, dense dynamic face geometry can be reconstructed from monocular RGB video [Thies et al. 2016]. Recently, Cao et al. [2016] proposed an image-based representation for dynamic 3D avatars that supports various hairstyles and parts of the upper body.

The ability to reconstruct face models from monocular video enables advanced video editing effects. Examples are re-arranging a database of video frames [Li et al. 2012] such that mouth motions match a new audio stream [Bregler et al. 1997; Taylor et al. 2015], face puppetry by reshuffling a database of video frames [Kemelmacher-Shlizerman et al. 2010], or re-rendering of an entire captured face model to make mouth motion match a dubbed audio-track [Garrido et al. 2015]. Other approaches replace the face identity in a target video [Dale

et al. 2011; Garrido et al. 2014]. When face expressions are modified, it is often necessary to re-synthesize the mouth and its interior under new or unseen expressions, for which image-based [Kawai et al. 2014; Thies et al. 2016] or 3D template-based [Thies et al. 2015] methods were examined. Vlasic et al. [2005] describe a model-based approach for expression mapping onto a target face video, enabling off-line reenactment of faces under controlled recording conditions. While Thies et al. [2015] enable real-time dense tracking and photo-realistic expression mapping between source and target RGB-D video, Face2Face [Thies et al. 2016] enables real-time face reenactment between captured RGB video of one actor and an arbitrary target face video. Under the hood, they use a real-time tracker capturing dense shape, appearance and lighting. Expression mapping and image-based mouth-re-rendering enables photo-realistic target appearance. None of the aforementioned capture and reenactment approaches succeeds under strong face occlusion by a VR headset, nor can combine data from several cameras – inside and outside the display – and thus cannot realistically re-render the eye region and appearance, including correct gaze direction.

Parts of our method are related to image-based eye-gaze estimation approaches. Commercial systems exist for eye gaze tracking of the unoccluded face using special externally placed cameras, e.g., from Tobii¹, or IR cameras placed inside a VR headset, e.g., from Pupil Labs². Appearance-based methods for gaze-detection of the unoccluded face from standard externally placed cameras were also researched [Sugano et al. 2014; Zhang et al. 2015]. Wang et al. [2016] simultaneously capture 3D eye gaze, head pose, and facial expressions using a single RGB camera at real-time rates. However, they solve a different problem from ours; we need to reenact – i.e., photo-realistically synthesize – the entire eye region appearance in a target video of either a different actor, or the same actor in a different lighting, from input video of an in-display camera. Parts of our method are related to gaze correction algorithms for teleconferencing where the eyes are re-rendered such that they look into the web-cam, which is typically displaced from the video display [Criminisi et al. 2003; Kuster et al. 2012; Kononenko and Lempitsky 2015]. Again, this setting is different from ours, as we need to realistically synthesize arbitrary eye region motions and gazes, and not only correct the frontal gaze direction.

Related to our paper is the work by Li et al. [2015] who capture moving facial geometry while wearing an HMD with an external depth sensor that is rigidly attached to the headset. In addition, they measure strain signals with electronic sensors to estimate facial expressions of regions hidden by the display. As a result, they obtain the expression coefficients of the face model which are used to animate virtual avatars. Recently, Olszewski et al. [2016] propose an approach for HMD users to control a digital avatar in real-time based on RGB data. The user’s mouth is captured by a camera that is rigidly attached to the HMD and a convolutional neural network is used to regress from the images to the parameters that control a digital avatar. They also track eyebrow motion based on a camera that is integrated into the head mounted display. Both of these approaches only allow to control a virtual avatar – rather than a real video – and do not capture the eye motion. Our approach takes this a step further and captures facial performance as well as the eye motion of a person using an HMD. In addition, we allow to re-render and reenact the face, mouth, and eye motion of a target stereo stream photo-realistically and in real-time. Note that our face tracking is also different since our camera is not attached to the HMD (i.e., we solve for the rigid head pose).

¹www.tobii.com

²www.pupil-labs.com

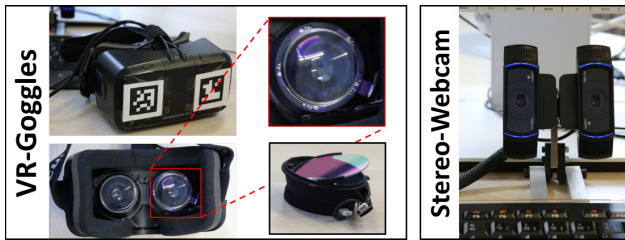


Figure 2: Hardware setups: a source actor experiences VR wearing an Oculus DK2 headset (left). We track the source actor using a commodity RGB-D sensor (front-facing), and augment the HMD with ArUco markers, as well as an IR webcam on the inside (mounted with Add-on Cups). The target actor footage is captured with a lightweight stereo rig, which is composed of two webcams (right).

3 Hardware Setup

For our method, we consider a source and a target actor. The *source actor* is wearing a head-mounted display (HMD), and we use a lightweight hardware setup to reconstruct and track the source actor’s face. To this end, we augment commodity VR goggles with a simple IR webcam on the inside for tracking one eye. For tracking the rigid pose and facial expressions, we use outside-in tracking with a real-time RGB-D sensor (Asus Xtion Pro), as well as ArUco AR markers on the front panel of the HMD.

The tracking and reconstruction pipeline for the *target actor* differs. Here, we use a lightweight stereo setup which is composed of two commodity webcams. This allows for robust face tracking and generation of 3D video content that we can display on the source actor’s HMD. We typically pre-record the target actor’s video stream, but we modify and replay it in real time. In addition, we assume that faces in the target video are mostly unoccluded.

In the following paragraphs, we detail the hardware configuration of our head-mounted display for source actor tracking, as well as the lightweight stereo rig for target actor tracking. Both setups are shown in Fig. 2.

3.1 Head-Mounted Display for the Source Actor

For visualizing 3D content to the source actor, we use an Oculus Rift DK2 visualization as a head-mounted display, and we integrate a simple IR webcam to track the source actor’s eyes. This camera is integrated inside the HMD with Oculus Rift DK2 Monocular Add-on Cups, which allows us to obtain a close-up camera stream of the right eye [Labs 2016]; see Fig. 2, left. Although we present results on this specific setup, our method is agnostic to the head-mounted display, and can be used in combination with any other VR device, such as the VR Box, Samsung Gear VR, or HTC Vive.

The monocular camera, which we integrate in the DK2, captures an IR stream of the eye region at a resolution of 640×480 pixels at 120Hz. IR LEDs are used as active light sources such that bright images can be obtained, and the camera latency is 5.7ms. The camera is mounted on the top of the VR device lens and an IR mirror is used to get a frontal view of the eye without interfering with the view on the display. The camera is located close to the lenses (see Fig. 2, left), and captures images \mathbf{I}_E of the eyes at real-time rates.

Note that our prototype has only one internal camera. Thus, we use the stream of the right eye only to infer and reenact the motion of both the left and the right eye. This is feasible as long as we can assume that the focus distance is the same as during calibration, that is eye vergence (squinting) does not change. If this assumption

does not hold, a second internal camera for the left eye can be easily integrated into our design.

In addition, we augment the DK2 by attaching two ArUco AR markers to the front of the HMD to robustly track the rigid pose. During face tracking, this allows us to decouple the rigid head pose from the facial expression parameters by introducing additional soft constraints obtained from the markers. The combination of marker tracking and joint optimization allows to further stabilize the estimates of the rigid head pose, leading to much higher tracking accuracy (see Fig. 5).

Tracking of the Source Actor For tracking the source actor in real-time, we use a commodity RGB-D camera. Specifically, we use an Asus Xtion Pro RGB-D sensor that captures RGB-D frames of 640×480 pixels at 30 fps (both color and depth). Every frame, the camera captures an RGB image \mathbf{I}_I and a depth image \mathbf{D} , which we assume to be spatially and temporally aligned. Both images are parametrized by pixel coordinates \mathbf{p} , each RGB value is $\mathbf{I}_I(\mathbf{p}) \in \mathbb{R}^3$, and the depth data is back-projected in camera space $\mathbf{D}_I(\mathbf{p}) \in \mathbb{R}^3$. Note that we are only considering visible pixel locations $\mathbf{p} \in \mathcal{P}$ on the face that are not occluded by the HMD.

3.2 3D Stereo Rig for Target Actor Tracking

In order to obtain a 3D reconstruction of the target actor, we use the binocular image stream of a lightweight stereo rig. Our setup is composed of two commodity webcams (Logitech HD Pro Webcam C920), which are rigidly mounted side-by-side and facing the same direction on a stereo bar; see Fig. 2, right. The camera rig synchronously captures a stereo stream of two RGB pairs $\mathbf{I}_I^{(c)}$, $c \in \{1, 2\}$ at real-time rates. The two cameras are synchronized up to 30ms and capture images at the resolution of 800×600 pixels at 30Hz. The captured stereo content is used to capture the target 3D video content. We calibrate the stereo rig intrinsically and extrinsically using standard OpenCV routines.

Note that we have also the option to track the target actor from a monocular stream (similar to Thies et al. [2016]); e.g., as shown in Fig. 8. However, our primary goal is the gaze-aware reenactment of a stereo stream which can be rendered on a 3D display (e.g., a VR device).

4 Synthesis of Facial Imagery

We parameterize human heads under general uncontrolled illumination based on a multi-linear face and an analytic illumination model. A linear PCA basis is used for facial identity [Bianz and Vetter 1999] (geometry and reflectance) and a blendshape basis for the expression variations [Alexander et al. 2009; Cao et al. 2014b]. This results in the spatial embedding of the underlying mesh and the associated per-vertex color information parameterized by linear model, $\mathcal{F}(\mathbf{T}, \alpha, \beta, \delta)$ and $\mathcal{C}(\beta, \gamma)$, respectively. The mesh has 106K faces and 53K vertices. Here, $\mathbf{T} \in \mathbb{R}^{4 \times 4}$ models the rigid head pose, $\alpha \in \mathbb{R}^{80}$ the geometric identity, $\beta \in \mathbb{R}^{80}$ the surface reflectance properties, $\delta \in \mathbb{R}^{78}$ the facial expression, and $\gamma \in \mathbb{R}^{3 \cdot 9}$ the incident illumination situation. The $3 \cdot 9$ illumination coefficients encode the RGB illumination based on 9 Spherical Harmonics (SH) [Ramamoorthi and Hanrahan 2001] basis functions. For convenience, we stack all parameters of the model in a vector $\mathcal{X} = (\mathbf{T}, \alpha, \beta, \delta, \gamma) \in \mathbb{R}^{265}$. Synthetic monocular images \mathbf{I}_S and synthetic stereo pairs $(\mathbf{I}_S^{(1)}, \mathbf{I}_S^{(2)})$ of arbitrary virtual heads can be generated by varying the parameters \mathcal{X} and using the GPU rasterization pipeline to simulate the image formation process. To this end, we use a standard pinhole camera model $\Pi(\bullet)$ under a full perspective projection.

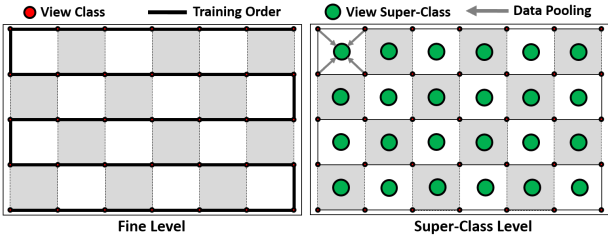


Figure 3: Left: the eye calibration pattern used to generate training data for learning our image-based eye-gaze retrieval. In the training phase, we progress row-by-row in a zig-zag order; each grid point is associated with a eye-gaze direction. Right: to obtain robust results, we perform a hierarchical classification where classes of the finer level are accumulated into a smaller set of super classes.

Mouth Interior The parametric head model does not contain rigged teeth, a tongue or a mouth interior, since these facial features are challenging to reconstruct and track from stereo input due to strong occlusions in the input sequence. Instead, we use an image-based retrieval strategy in the spirit of Thies et al. [2016] to find suitable mouth frames in a training sequence. This retrieval is based on a dense appearance graph that allows us to obtain a good match to the queried expression and leads to temporally coherent results. The output of this step is then composited with the rendered model using alpha blending.

Eyeball and Eyelids We use a unified image-based strategy to synthesize plausible animated eyes (eyeball and eyelid) that can be used for photo-realistic facial reenactment in VR applications. This novel strategy is one of the main contributions of this work and is described in more detail in the next section.

5 An Image-based Eye and Eyelid Model

We propose a novel image-based retrieval approach to track and synthesize the region of the eyes, including eyeballs and eyelids. This approach is later used in all presented applications, namely gaze correction for video calls (see Sec. 8.1), gaze-aware facial reenactment (see Sec. 8.2) and video conferencing in VR (see Sec. 8.3). We chose an image-based strategy since it is specific to a person; it not only models the behavior of the eyeballs, but also captures idiosyncrasies of eyelid movement while enabling photo-realistic re-rendering. Our approach uses a hierarchical variant of random ferns [Ozuysal et al. 2010] to robustly track the eye region. To this end, we propose a novel actor-specific and fully automatic training stage. In the following, we describe our fully automatic data generation process, the used classifier and the optimizations that are required to achieve fast, robust, and temporally stable gaze estimates.

5.1 Training Data Generation

To train our image-based eye regression strategy, we require a sufficiently large set of labeled training data. Since manual data annotation for every new user is practically infeasible, we propose a very efficient approach based on a short eye calibration sequence.

During the training process, we display a small circle at different positions of a 7×5 -tiled image grid on the screen in front of the user; see Fig. 3, left. This allows us to capture the space of all possible look-at points on the display. In addition, we capture an image of a closed eye for the synthesis of eye blinks. The captured image data \mathcal{I}_n is divided into $36 = 7 \times 5 + 1$ unique classes l_n ,

where every class is associated with a view direction. The ground truth gaze directions are given by the current position of the *dot* on the screen in the training data. During training, the user focuses on the displayed dot with his eye gaze. We show every dot for 2 seconds for each location. The data captured in the first 0.4 seconds is rejected to allow the user a grace period to adjust his eye-gaze to new positions. In the remaining 1.6 seconds, we capture 50 frames which we use to populate the corresponding class. After that, we proceed to the next class, and move the dot to the next position. Note that the dot location for a given class is fixed, but we obtain multiple samples within each class (one for each frame) from the input data. This procedure progresses row-by-row in a zig-zag order; see Fig. 3, left. Finally, we augment the samples in each class by jittering each captured source image by ± 1 pixels, resulting in 9×50 training frames per class.

Each cluster is also associated with a representative image of the eye region obtained from the captured input data. The representative image of each class is given by the median of the corresponding video clip, which is later used for the synthesis of new eye movements. Finally, we add an additional class which represents eye blinks; this class is obtained by asking the user to close his eyes at the end of the training phase. This calibration sequence is performed for both the source and target actor. Since the calibration sequence is the same for both actors, we obtain one-to-one correspondences between matching classes across actors. As detailed in the following subsections, this allows us to train an eye-gaze classifier which predicts gaze directions for the source actor at runtime. Once trained, for a given source input frame, the classifier identifies cluster representatives from the target actor. The ability to robustly track the eye direction of the source actors forms the basis for real-time gaze-aware facial reenactment; i.e., we are able to photo-realistically animate/modify the eyes of a target actor based on a captured video stream of the source actor. In the following, we detail our eye tracking strategy.

5.2 Random Ferns for Eye-gaze Classification

The training data $\{\mathcal{I}_n, l_n\}_{n=1}^N$, which is obtained as described in the previous section, is a set of N input images \mathcal{I}_n with associated class labels l_n . Each label $l_n \in \{c_l\}_{l=1}^C$ belongs to one of C classes c_l . In our case, the images of the eye region are clustered based on gaze direction. We tackle the associated supervised learning problem by an ensemble of M random ferns [Ozuysal et al. 2010], where each fern is based on S features. To this end, we define a sequence of $K = MS$ binary intensity features $\mathbf{F} = \{f_k\}_{k=1}^K$ which is split into M independent subsets \mathbf{F}_m of size S . Assuming statistical independence and applying *Bayes Rule*, the log-likelihood of the class label posterior can be written as:

$$\log P(c_l|\mathbf{F}) \sim \log \left[P(c_l) \cdot \prod_{m=1}^M P(\mathbf{F}_m|c_l) \right].$$

The class likelihoods $P(\mathbf{F}_m|c_l)$ are learned using random ferns. Each fern performs S binary tests [Ozuysal et al. 2010], which discretizes the per-class feature likelihood into $B = 2^S$ bins. At first, we initialize all bins with one to prevent taking the logarithm of zero. In all experiments, we use $M = 800$ ferns with $S = 5$ binary tests. Finally, the class with the highest posterior probability is chosen as the classification result. Training takes only around 4.9ms per labeled image, thus training runs in parallel to the calibration sequence. Once trained, the best class can be obtained in less than 1.4ms.

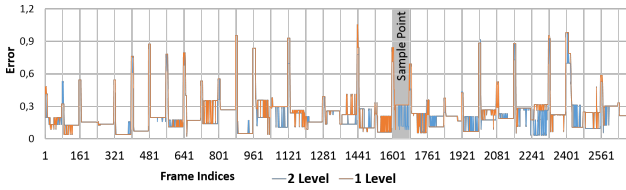


Figure 4: Comparison of a one and a two level classifier. Ground truth data is obtained by a test subject looking at a dot that appears every 80 frames (2.6 seconds) at random; error is measured in normalized screen space coordinates in $[0, 1]^2$. As shown by the magnitude of the positional error, the multi-level classifier obtains higher accuracy.

5.3 Hierarchical Eye-gaze Classification

In order to efficiently handle classification outliers, we perform eye-gaze classification on a two-level hierarchy with a fine and a coarse level. The $35 + 1$ classes of the fine level are defined by the grid points of the zig-zag calibration pattern shown in Fig. 3, left. To create the coarse level, we merge neighboring classes of the fine level into superclasses. For a set of four adjacent classes (overlap of one), we obtain one superclass; see Fig. 3, right. This leads to a grid with $25 = 4 \times 6 + 1$ unique classes (rather than the $35 + 1$ classes; the class for eye blink is kept the same).

During training, we train the two hierarchy levels independently. The training data for the fine level is directly provided by the calibration pattern, and the data for the coarse level is inferred as described above. At test time, we first run the classifier of the coarse level which provides one of the superclasses. Then the classification on the fine level only considers the four classes of the best matching superclass.

The key insight of this coarse-to-fine classification is to break up the task into easier sub-problems. That is, the classification on the coarse level is more robust and less prone to outliers of the fern predictions since there are fewer classes to distinguish between. The fine level then complements the superclass prediction by increasing the accuracy of the inferred eye-gaze directions. In the end, this multi-level classifier leads to high accuracy results while minimizing the probability of noisy outliers. In Fig. 4, we show a comparison between a one and two level classifier. The two level approach obtains a lower error (mean 0.217973, std.dev. 0.168094) compared to the one level approach (mean 0.24036, std.dev. 0.18595).

5.4 Temporal Stabilization of Classification Results

In the previous sections, we introduced a classifier that infers the eye-gaze direction from a single RGB frame – or monochromatic IR frame in the case of the HMD camera – without the assumption of a temporal prior. Due to the probabilistic nature of random ferns, the classification results are sometimes temporally unstable. In practice, this can lead to jitter even in the absence of eye motion.

In order to alleviate this problem, we introduce a temporal stabilizer that favors the previously-retrieved eye-gaze direction. This particularly helps in the case of small eye motions, where the switch to a new class would introduce unwanted jitter. To this end, we adjust the likelihood of a specific class $P(c_t)$ using a temporal prior such that the previously-predicted eye-gaze direction c_{old} is approximately $1.05 \times$ more likely than changing the state and predicting a different class:

$$P(c_t) = \begin{cases} 0.513, & \text{if } (c_t = c_{old}) \\ 0.487, & \text{else} \end{cases} .$$

We integrate the temporal stabilization on both levels of the classification hierarchy. First, we *favor* the super class on the coarse level using the aforementioned temporal prior. If the current and previous prediction on the coarse level are the same, we apply P_{prior} to the view within the superclass in the same fashion. Otherwise, we use no temporal bias on the fine level. This allows fast jumps of the eye direction, which is crucial for fast saccade motion that pushes the boundary of the 30Hz temporal resolution of the stereo setup.

6 Parametric Model Fitting

Our approach uses two different tracking and reconstruction pipelines for each (source and target) actor, respectively. The source actor, who is wearing the HMD, is captured using an RGB-D camera; see Sec. 3.1. Here, we constrain the face model \mathcal{F} by the visible pixels on the face that are not occluded by the HMD, as well as the attached ArUco AR markers. The target actor reconstruction – which becomes the corresponding VR target content that is animated at runtime – is obtained in a pre-process with the lightweight stereo setup described in Sec. 3.2. For both tracking pipelines, we use an *analysis-by-synthesis* approach to find the model parameters \mathcal{X} that best explain the input observations. The underlying inverse rendering problem is tackled based on energy minimization. For simplicity, we first describe the energy formulation for tracking the target actor in Sec. 6.1. Then, we introduce the objective function for fitting the face model of the source actor in Sec. 6.2.

6.1 Target Actor Energy Formulation

In order to process the stereo video stream of the target actor, we introduce a model-based stereo reconstruction pipeline that constrains the face model according to both RGB views per frame. That is, we aim to find the optimal model parameters \mathcal{X} constrained by the input stereo pair $\{\mathbf{I}_T^{(c)}\}_{c=1}^2$.

Our model-based stereo reconstruction and tracking energy E_{target} is a weighted combination of alignment and regularization constraints:

$$E_{target}(\mathcal{X}) = \underbrace{[w_{ste} E_{ste}(\mathcal{X}) + w_{lan} E_{lan}(\mathcal{X})]}_{\text{alignment}} + \underbrace{[w_{reg} E_{reg}(\mathcal{X})]}_{\text{regularizer}} . \quad (1)$$

We use dense photometric stereo alignment E_{ste} and sparse stereo landmark alignment E_{reg} in combination with a robust statistical regularization strategy E_{reg} . The sub-objectives of E_{target} are scaled based on empirically determined, but constant, weights $w_{ste} = 100$, $w_{lan} = 0.0005$, and $w_{reg} = 0.0025$ that balance the relative importance.

Dense Photometric Stereo Alignment We enforce dense photometric alignment to both views in the stereo pair. For robustness against outliers, we use the $\ell_{2,1}$ -norm [Ding et al. 2006] instead of a traditional least-squares formulation:

$$E_{ste}(\mathcal{X}) = \sum_{c=1}^2 \frac{1}{|\mathcal{P}^{(c)}|} \sum_{\mathbf{p} \in \mathcal{P}^{(c)}} \left\| \mathbf{I}_S^{(c)}(\mathbf{p}) - \mathbf{I}_T^{(c)}(\mathbf{p}) \right\|_2 . \quad (2)$$

Here, $\mathcal{P}^{(c)}$ is the set of visible model pixels \mathbf{p} from the c^{th} -camera. The visible pixels of the model are determined by a forward rendering pass using the old parameters. We normalize based on the total number of pixels $|\mathcal{P}^{(c)}|$ to guarantee that both views have the same influence. Note that the two sets of visible pixels are updated in every optimization step, and for the forward rendering pass we use the face parameters of the previous iteration or frame.

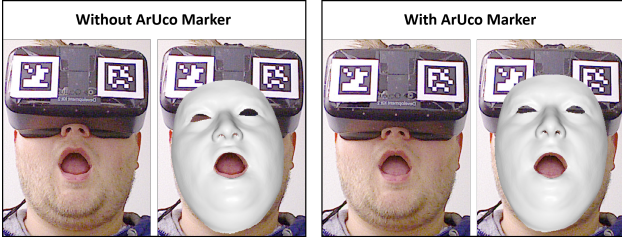


Figure 5: Tracking with and without ArUco Marker stabilization.

Sparse Stereo Landmark Alignment We use sparse point-to-point alignment constraints in 2D image space that are based on per-camera sets $\mathcal{L}^{(c)}$ of 66 automatically detected facial landmarks. The landmarks are obtained by the detector of Saragih et al. [2011]:

$$E_{\text{lan}}(\mathcal{X}) = \sum_{c=1}^2 \frac{1}{|\mathcal{L}^{(c)}|} \sum_{(1,k) \in \mathcal{L}^{(c)}} w_{1,k} \|1 - \Pi(\mathcal{F}_k(\mathbf{T}, \boldsymbol{\alpha}, \boldsymbol{\beta}, \boldsymbol{\delta}))\|_2^2. \quad (3)$$

The detected 2D features \mathbf{l} are enforced to be spatially close to the projected corresponding vertex $\mathcal{F}_k(\mathbf{T}, \boldsymbol{\alpha}, \boldsymbol{\beta}, \boldsymbol{\delta})$. Constraints are weighted by the confidence measures $w_{1,k}$, which are provided by the sparse facial landmark detector.

Statistical Regularization In order to avoid implausible face fits, we apply a statistical regularizer to the unknowns of \mathcal{X} that are based on our parametric face model. We favor plausible faces where parameters are close to the mean with respect to their standard deviations σ_{id} , σ_{alb} , and σ_{exp} .

$$E_{\text{reg}}(\mathcal{X}) = \sum_{i=1}^{80} \left[\left(\frac{\alpha_i}{\sigma_{\text{id},i}} \right)^2 + \left(\frac{\beta_i}{\sigma_{\text{alb},i}} \right)^2 \right] + \sum_{i=1}^{76} \left(\frac{\delta_i}{\sigma_{\text{exp},i}} \right)^2. \quad (4)$$

6.2 Source Actor Tracking Objective

At runtime, we track the source actor who is wearing the HMD and is captured by the RGB-D sensor. The tracking objective for visible pixels that are not occluded by the HMD is similar to the symmetric point-to-plane tracking energy in Thies et al. [2015]. In addition to this, we introduce rigid stabilization constraints which are given by the ArUco AR markers in front of the VR headset. These constraints are crucial to robustly separate the rigid head motion from the face identity and pose parameters (see Fig. 5). The total energy for tracking the target actor at runtime is given by the following linear combination of residual terms:

$$E_{\text{source}}(\mathcal{X}) = w_{\text{rgb}} E_{\text{rgb}}(\mathcal{X}) + w_{\text{geo}} E_{\text{geo}}(\mathcal{X}) + w_{\text{sta}} E_{\text{sta}}(\mathcal{X}) + w_{\text{reg}} E_{\text{reg}}(\mathcal{X}). \quad (5)$$

The first term of this objective E_{rgb} measures the photometric alignment of the input RGB image $\mathbf{I}_{\mathcal{I}}$ from the camera and the synthetically-generated rendering $\mathbf{I}_{\mathcal{S}}$:

$$E_{\text{rgb}}(\mathcal{X}) = \frac{1}{|\mathcal{P}|} \sum_{\mathbf{p} \in \mathcal{P}} \|\mathbf{I}_{\mathcal{S}}(\mathbf{p}) - \mathbf{I}_{\mathcal{I}}(\mathbf{p})\|_2. \quad (6)$$

This color term is defined over all visible pixels \mathcal{P} in the bottom half of the face that are not occluded by the HMD, and we use the same $\ell_{2,1}$ -norm as in Eq. 2.

In addition to the photometric alignment, we constrain the face model by the captured range data:

$$E_{\text{geo}}(\mathcal{X}) = w_{\text{point}} E_{\text{point}}(\mathcal{X}) + w_{\text{plane}} E_{\text{plane}}(\mathcal{X}). \quad (7)$$

Similar to E_{rgb} , geometric residuals of E_{geo} are defined over the same set of visible pixels on the face. The geometric term is composed of two sub-terms, a point-to-point E_{point} term, where $\mathbf{D}_{\mathcal{I}}$ is the input depth and $\mathbf{D}_{\mathcal{S}}$ is the rendered depth (both are back-projected into camera space),

$$E_{\text{point}}(\mathcal{X}) = \sum_{\mathbf{p} \in \mathcal{P}} \|\mathbf{D}_{\mathcal{S}}(\mathbf{p}) - \mathbf{D}_{\mathcal{I}}(\mathbf{p})\|_2^2, \quad (8)$$

as well as a symmetric point-to-plane term

$$E_{\text{plane}}(\mathcal{X}) = \sum_{\mathbf{p} \in \mathcal{P}} [d_{\text{plane}}^2(N_{\mathcal{S}}(\mathbf{p}), \mathbf{p}) + d_{\text{plane}}^2(N_{\mathcal{I}}(\mathbf{p}), \mathbf{p})], \quad (9)$$

where $d_{\text{plane}}(\mathbf{n}, \mathbf{p}) = [(\mathbf{D}_{\mathcal{S}}(\mathbf{p}) - \mathbf{D}_{\mathcal{I}}(\mathbf{p}))^T \cdot \mathbf{n}]$, $N_{\mathcal{I}}(\mathbf{p})$ is the input normal and $N_{\mathcal{S}}(\mathbf{p})$ the rendered model normal.

In addition to the constraints given by the raw RGB-D sensor data, the total energy of the source actor E_{source} incorporates rigid head pose stabilization. This is required, since in our VR scenario the upper part of the face is occluded by the HMD. Thus, only the lower part can be tracked and the constraints on the upper parts of the face, which normally stabilize the head pose, are missing. To stabilize the rigid head pose, we use the two ArUco markers that are attached to the front of the HMD (see Fig. 2, left).

We first extract a set of eight landmark locations based on the two markers (four landmarks each). In order to handle noisy depth input, we fit two 3D planes to the frame’s point cloud that bound each marker, respectively. We then use the resulting 3D corner positions of the markers, and project them into face model space. Using these reference positions A_k we establish the rigid head stabilization energy E_{sta} :

$$E_{\text{sta}}(\mathcal{X}) = \frac{1}{|\mathcal{S}|} \sum_{(1,k) \in \mathcal{S}} \|1 - \Pi(\mathbf{T}A_k)\|_2^2. \quad (10)$$

Here, \mathcal{S} defines the correspondences between the detected 2D landmark positions \mathbf{l} in the current frame and the reference positions A_k . In contrast to the other data terms, E_{sta} depends only on the rigid transformation \mathbf{T} of the face and replaces the facial landmark term used by Thies et al. [2015]. Note that the Saragih tracker is unable to robustly track landmarks in this scenario since only the lower part of the face is visible. The statistical regularization term E_{reg} is the same as for the target actor (see Eq. 4).

6.3 Data-Parallel Optimization

We find the optimum of both face tracking objectives $\mathcal{X}_{\text{source}}^* = \text{argmin}_{\mathcal{X}} E_{\text{source}}(\mathcal{X})$ and $\mathcal{X}_{\text{target}}^* = \text{argmin}_{\mathcal{X}} E_{\text{target}}(\mathcal{X})$ based on variational energy minimization, leading to an unconstrained non-linear optimization problem. Due to the robust $\ell_{2,1}$ -norm used to enforce photo-metric alignment, we find the minimum based on a data-parallel *Iteratively Re-weighted Least Squares* (IRLS) solver [Thies et al. 2016]. At the heart of the IRLS solver, a sequence of non-linear least squares problems are solved with a GPU-based *Gauss-Newton* approach [Zollhöfer et al. 2014; Wu et al. 2014; Zollhöfer et al. 2015; Thies et al. 2015; DeVito et al. 2016; Thies et al. 2016] that builds on an iterative Preconditioned Conjugate Gradient (PCG) solver. The optimization is run in a coarse-to-fine fashion using a hierarchy with three levels. We only run tracking on

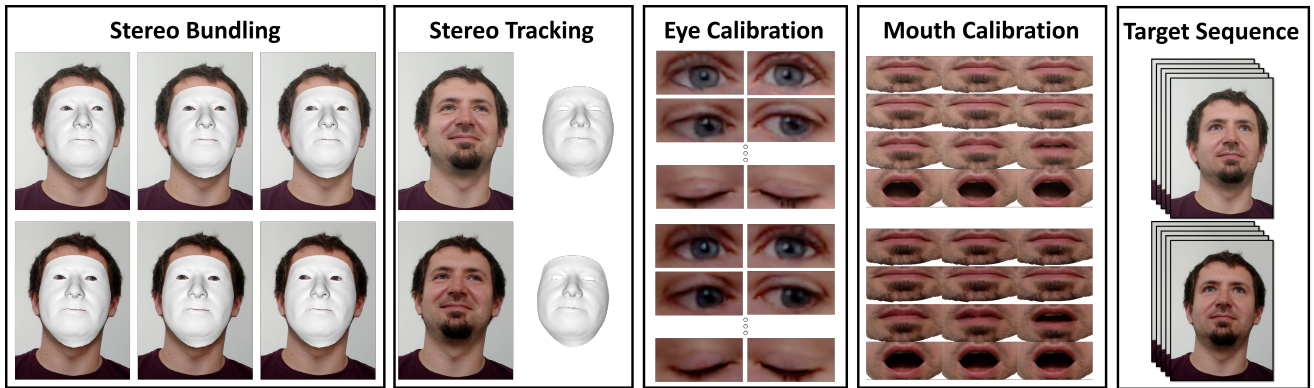


Figure 6: Building a personalized stereo avatar; from left to right: we first jointly optimize for all unknowns of our parametric face model using a non-rigid bundle adjustment formulation on the input of three stereo pairs. For tracking, we only optimize for expression, lighting, and rigid pose parameters constrained by synchronized stereo input; this optimization run in real-time. Next, we train our data-driven eye tracker with data from an eye-calibration sequence. In addition to eye calibration, we build a database of mouth stereo pairs which captures the variation of mouth motion. As a result, we obtain a tracked stereo target, which is used during live re-enactment (this is the target actor).

the two coarser levels using seven IRLS steps on the coarsest and one on the medium level. For each IRLS iteration, we perform one GN step with four PCG steps. In order to exploit temporal coherence, we initialize the face model with the optimization results from the previous frame. First, this gives us a good estimate of the visible pixel count in the forward rendering pass, and second, it provides a good starting point for the GN optimization. Note that we never explicitly store $J^T J$, but instead apply the multiplication of the Jacobian (and its transpose) on-the-fly within every PCG step. Thus, the compute cost for each PCG iteration becomes more expensive for multi-view optimization of E_{target} ; although materialization is still less efficient, since we only need a small number of PCG iterations. In addition to optimizing for the parameters of the face model, we jointly optimize for the spherical harmonics coefficients. Since we use three bands, this involves 27 unknowns for the lighting (three per RGB channel); cf. Sec. 4.

7 Face Rig and Compositing

Generation of a Personalized Face Rig At the beginning of each recording, both of the source and target actor, we compute a person-specific face rig in a short initialization stage. To this end, we capture three keyframes with slightly different head rotations in order to recover the user’s facial geometry and skin reflectance. Given the constraints of these three keyframes, we jointly optimize for all unknowns of our face model \mathcal{F} – facial geometry, skin reflectance, illumination, and expression parameters – using our tracking and reconstruction pipeline. Fig. 6 (left) shows this process for the stereo reconstruction pipeline. This initialization requires a few seconds to complete; once computed, we maintain a fixed estimate of the facial geometry and replace the reflectance estimate with person-specific illumination-corrected texture maps. In the stereo case, we compute one reflectance texture for each of the two cameras. This ensures that the two re-projections exactly match the input streams, even if the two used cameras have slightly different color response functions. In the following steps, we use this high-quality stereo albedo map for tracking, and we restrict the optimizer to only compute the per-frame expression and illumination parameters. All other unknowns (e.g., geometry) are person-specific and can remain fixed for a given user.

In order to enable high-quality reenactment of the mouth and the eye/eyelids in the target video, we provide two additional short calibration sequences (each a few seconds); see Fig. 6 (right). First,

the user slowly opens and closes his mouth in front of the sensor. This allows us to generate a mouth-motion database following Thies et al. [2016]. At runtime, we use the mouth calibration to synthesize realistic textures for the mouth interior and teeth. Since we record stereo mouth frames, we can retrieve coherent mouth-frame pairs and visualize the result on a 3D display. Second, we capture the person-specific appearance and motion of the eyes and eyelids during the initialization stage. The obtained eye-calibration data is then used for training our eye tracker (cf. Sec. 5).

Real-time Compositing and Facial Reenactment At run-time, we use the reconstructed face model along with its calibration data (eye and mouth) to photo-realistically re-render the face of the target actor. We first modify the facial expression parameters of the reconstructed face model of the target actor. The expressions are transferred from source to target in real-time using the subspace deformation transfer approach of Thies et al. [2016]. Based on the modified face parameters, the corresponding mouth frame is retrieved by selecting the closest frame in the mouth database with respect to a photo-metric and parametric similarity measure [Thies et al. 2016]. Since our eye gaze estimator allows a one-to-one correspondence between the source and the target actor, we also know the index of the gaze class in the eye database of the target actor. The rendering pipeline is similar to Thies et al. [2016]: on top of the target video, we first render the reprojected and illumination corrected mouth texture, the eye texture and then the (potentially modified) 3D face model based on its parameters under the estimated illumination of the target video using alpha blending. Note that for the stereo rendering pipeline, we retrieve consistent mouth and eye frame pairs to facilitate visualization on a 3D display.

8 Results

In this section, we evaluate our gaze-aware facial reenactment approach in detail and compare against state-of-the-art reenactment methods. All experiments run on a desktop computer with an Nvidia GTX980 and a 3.3GHz Intel Core i7-5820K processor. For tracking the source and target actor, we use our hardware setup as described in Sec. 3. However, note that our method is agnostic to the specific hardware components such as the VR headset. Our approach is robust to the specific choice of parameters, and we use a fixed parameter set in all experiments. For stereo tracking, we set the following weights in our energy formulation: $w_{\text{ste}} = 100.0$, $w_{\text{lan}} = 0.0005$,

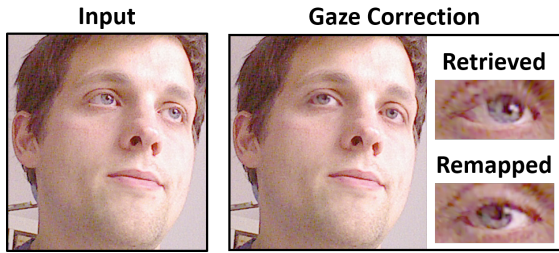


Figure 7: Gaze Correction: a common problem in video chats is the discrepancy between the physical location of the webcam and the screen, which leads to unnatural eye appearance (left). We use our eye tracking and retrieval strategy to correct the gaze direction in such a scenario, thus enabling realistic video conversations with natural eye contact (right).

$w_{\text{reg}} = 0.0025$. Our RGB-D tracking approach uses $w_{\text{rgb}} = 100.0$, $w_{\text{geo}} = 10000.0$, $w_{\text{sta}} = 1.0$, $w_{\text{reg}} = 0.0025$.

As our main results, we demonstrate three distinct applications for our real-time gaze-aware facial reenactment approach: gaze correction in live video footage, gaze-aware facial reenactment, and self-reenactment for VR goggles removal. All three applications share a common initialization stage that is required for the construction of a personalized face and eye/eyelid model of the users; see Sec. 7. The source video content is always captured using the Asus Xtion depth sensor. Depending on the application, we use our lightweight stereo rig (3D-stereo content; visualized as anaglyph) or the RGB-D sensor (standard video content).

8.1 Gaze Correction for Video Conferencing

Video conference calls, such as Skype chats, suffer from lack of eye contact between participants due to the discrepancy between the physical location of the camera and the screen. To address this common problem, we apply our face tracking and reenactment approach to the task of online gaze correction for live video footage; see Fig. 7. Our goal is the photo-realistic modification of the eye motion in the input video stream using our image-based eye and eyelid model. To this end, we densely track the face of the user, and our eye-gaze classifier provides us with an estimate of the gaze direction; i.e., we determine the 2D screen position where the user is currently looking. Given the eye tracking result, we modify the look-at point by applying a delta offset to the gaze direction which corrects for the different positions of the camera and screen. Finally, we retrieve a suitable eye texture that matches the new look-at point and composite it with the input video stream to produce the final output. A gaze correction example is shown in Fig. 7.

8.2 Gaze-aware Facial Reenactment

Our approach enables real-time photo-realistic and gaze-aware facial reenactment of monocular RGB-D and 3D stereo videos; see Fig. 8 and 10. In both scenarios, we track the facial expressions of a source actor using an external Asus Xtion RGB-D sensor, and transfer the facial expressions – including eye motion – to the video stream of a target actor. The eye motion is tracked using our eye-gaze classifier based on the data captured by the external camera (monocular RGB-D reenactment) or the internal IR camera which is integrated into the HMD (stereo reenactment). We transfer the tracked facial motion to a target video stream using the presented (stereo) facial reenactment approach. The modified eye region is synthesized using our unified image-based eye and eyelid model. The re-rendering and compositing is detailed in Sec. 7. This allows the source actor to

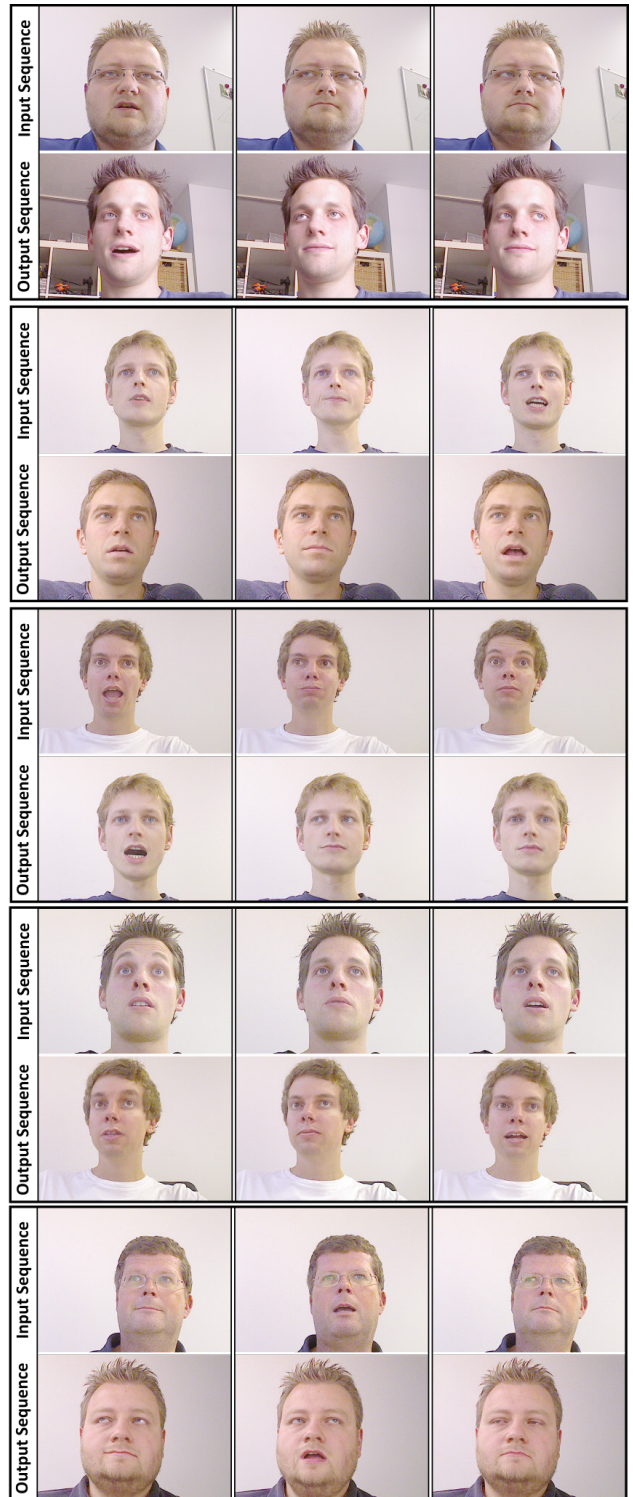


Figure 8: Gaze-aware facial reenactment of monocular RGB-D videos streams: we employ our real-time performance capture and eye tracking approach in order to modify the facial expressions and eye motion of a target video. In each sequence, the source actor's performance (top) is used to drive the animation of the corresponding target video (bottom).

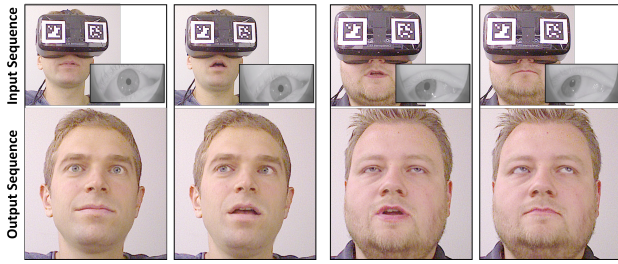


Figure 9: Self-Reenactment for VR Video Conferences: our real-time facial reenactment approach allows to virtually remove the HMD by driving a pre-recorded target video of the same person.

take full control of the face expression and eye gaze of the target video stream at real-time frame rates.

8.3 Self-Reenactment for VR Video Conferencing

Our real-time facial reenactment approach can be used to facilitate natural video chats in virtual reality. The major challenge for video conferencing in the VR context is that the majority of the face is occluded; thus, the other person in a VR conversation is unable to see the eye region. Rather than re-enacting different target actors with our facial reenactment method, we can self-reenact the source actor. Hence, our approach enables users to drive a pre-recorded target stereo video stream of themselves, which does not include the HMD. Using self-reenactment, the users can alter both the facial expression and the eye/eyelid motion of the pre-recorded video stream. This virtually removes the HMD from the face and allows users to appear as themselves in VR without suffering from occlusions due to the head mounted display; see Fig. 9. In addition, the output video stream mimics the eye motion, which is crucial since natural eye contact is essential in conversations. Note that the user can drive either a mono or a stereo video stream.

Although compression is not the main focus of this paper, it is interesting to note that the reenactment results can be easily transferred over a network with low bandwidth. In order to transmit the 3D video content at runtime to the other participants in a video chat, we only have to send the model parameters, as well as the eye and mouth class indices. The final modified stereo video can be directly synthesized on the receiver side using our photo-realistic re-rendering. Given that current video chat software, such as Skype, still struggles under poor network connections, we believe our reenactment may open up interesting possibilities.

8.4 Evaluation of Eye Tracking Accuracy

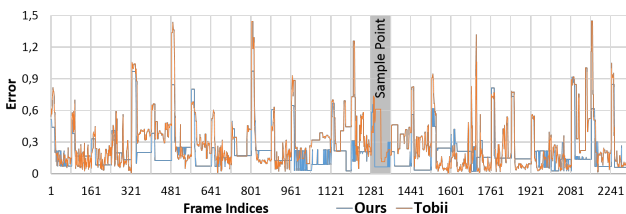


Figure 11: Comparison to the commercial Tobii EyeX eye tracking solution. The ground truth data is obtained by a test subject looking at a dot on the screen that appears every 80 frames (2.6 seconds) at different, random, normalized screen space coordinates in $[0, 1]^2$. We plot the magnitude of the positional error of Tobii EyeX and our approach. Our approach obtains a consistently lower error.

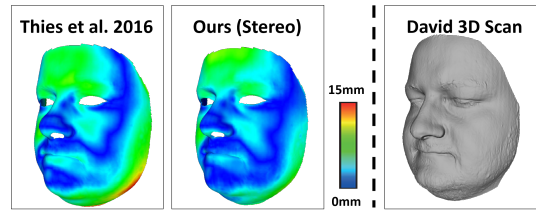


Figure 12: Accuracy of reconstructed identity: we compare our result against Face2Face [Thies et al. 2016]. Note that our approach obtains a better shape estimate of the chin, nose, and cheek regions. For reference, we use a structured light reconstruction from a David 3D scanner. The mean Hausdorff Distance of Face2Face is 3.751mm (RMS 4.738mm). Our approach has a mean distance of 2.672mm (RMS 3.384mm).

We evaluate the accuracy of our monocular eye gaze classification strategy on ground truth data and compare to the commercial Tobii EyeX eye tracker³. To this end, a test subject looks at a video sequence of a dot that is displayed at random screen positions for 80 successive frames (2.6 seconds given 30Hz input) – this provides a ground truth dataset. During this test sequence, we capture the eye motion using both the Tobii EyeX tracker and our approach. We measure the per-frame magnitude of the positional 2D error of Tobii and our approach with respect to the known ground truth screen positions; see Fig. 11. Note that screen positions are normalized to $[0, 1]^2$ before comparison. As can be seen, we obtain consistently lower errors. On the complete test sequence (more than 74 seconds), our approach has a mean error of 0.206 (std. dev. 0.178). In contrast, the Tobii EyeX tracker has a higher error of 0.284 (std. dev. 0.245). The high accuracy of our approach is crucial for realistic and convincing eye reenactment results.

8.5 Evaluation of Face Identity Estimation

The identity of the target actor is obtained using our model-based stereo bundle adjustment strategy. We compare our identity estimate with the approach of Thies et al. [2016] (Face2Face); see Fig. 12. As a reference, we use a high-quality structured light scan of the same person taken with a David 3D scanner. Our approach obtains a better reconstruction of the identity, especially the chin, nose, and cheek regions are of higher quality. Note that we estimate the identity by model-based bundle adjustment over the stereo pairs of three distinct time steps. Face2Face uses only the three images of one of the two RGB cameras.

8.6 Evaluation of Face Tracking Accuracy

In Fig. 13, we evaluate the stereo alignment accuracy of our approach and compare to the monocular face tracker of Face2Face [Thies et al. 2016]. As input, we use the binocular image stream captured by our custom stereo setup; see Sec. 3. We measure the photometric error between the input frames and the re-projection of the tracked face model. The tracking of Face2Face is based on the left camera stream, since this approach uses only monocular input data. Thus, Face2Face obtains a good fit with respect to the left camera (average error of 0.011), but the re-projection regarding the right camera suffers from strong misalignments (average error of 0.019). In contrast, our stereo tracking approach obtains consistently low errors for both views (average error of 0.011 left and 0.012 right), since we directly optimize for the best stereo overlap. For the aforementioned reenactment applications in VR, it is crucial to obtain high-quality alignment with respect to both camera streams of the stereo setup.

³www.tobii.com/xperience/

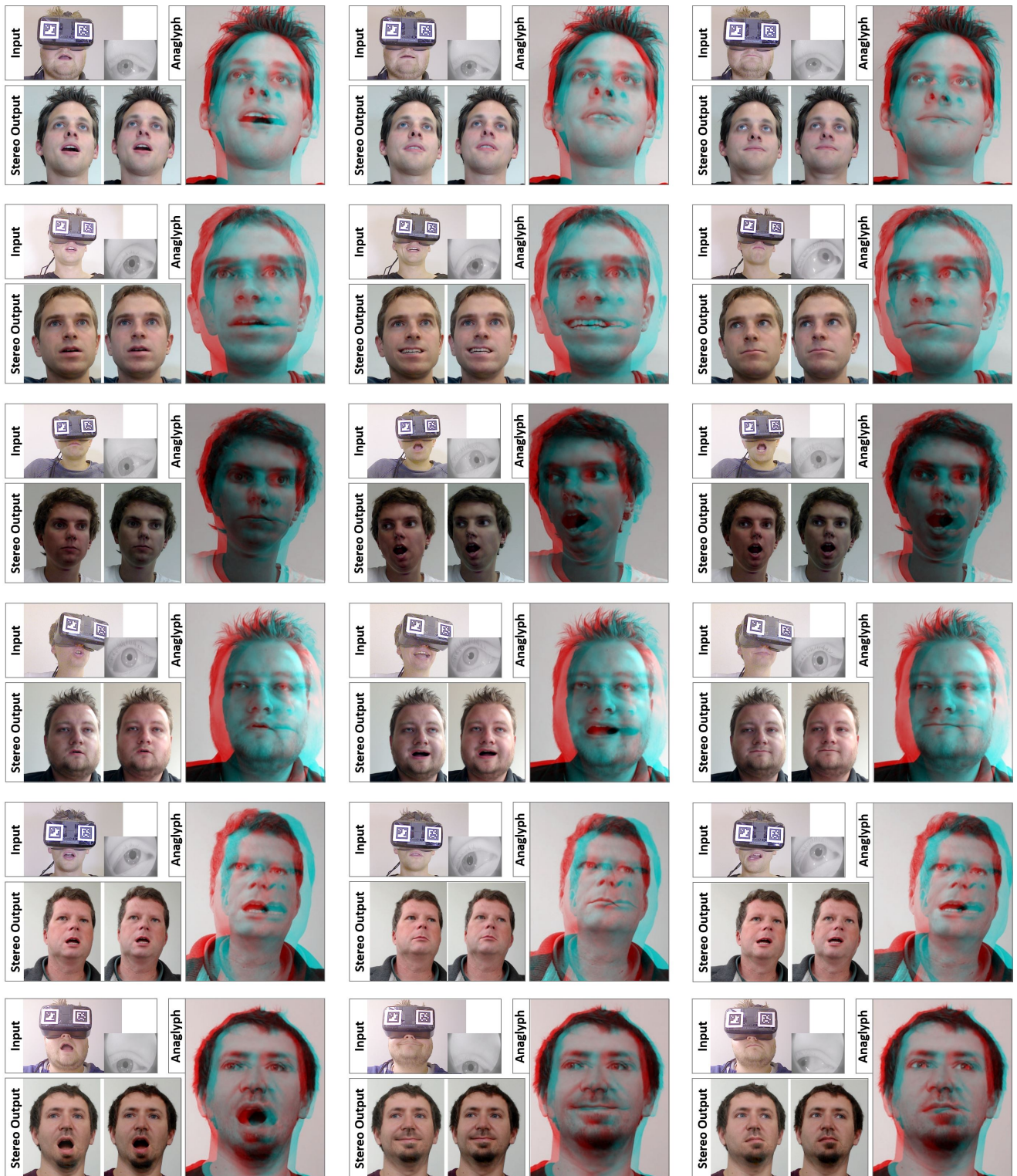


Figure 10: Gaze-aware facial reenactment of stereo target video content. We employ our real-time gaze-aware facial reenactment approach to modify the facial expressions and eye motion of stereo 3D content. The input (i.e., source actor) is captured with a frontal view and an internal IR camera. With our method, we can drive the facial animation of the stereo output videos shown below the input – the facial regions in these images are synthetically generated. The final results are visualized as anaglyph images on the right.

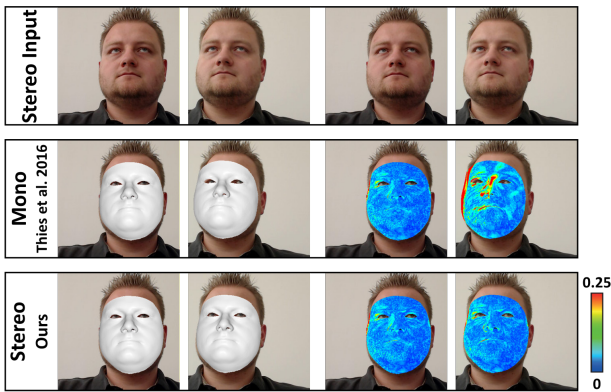


Figure 13: Stereo alignment: we compare the photometric accuracy of our approach to Face2Face [2016]. Face2Face only obtains a good fit to the image captured by the left camera (average error of 0.011), but the re-projection to the right camera suffers from strong misalignments (average error of 0.019). In contrast, our stereo tracking method obtains consistently low errors for both views (average error of 0.011 left and 0.012 right).

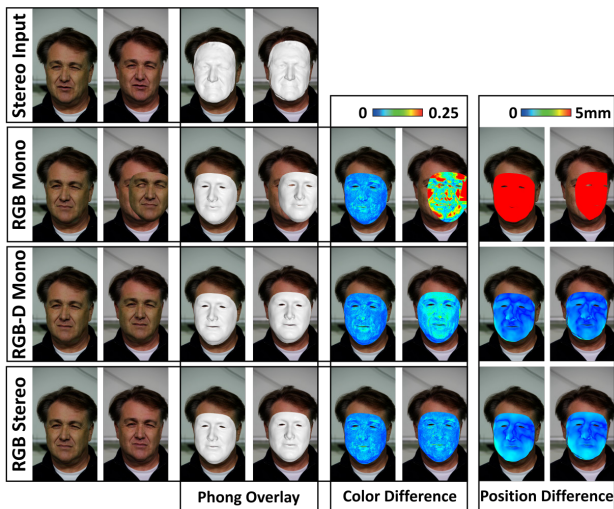


Figure 14: Ground truth comparison: we evaluate the photometric and geometric accuracy of our stereo tracking approach (RGB Stereo). As ground truth, we employ the high-quality stereo reconstructions of Valgaerts et al. [2012]. Our approach achieves consistently low photometric and geometric error for both views. We also compare to Thies et al. [2015] (RGB-D Mono) and Face2Face [2016] (RGB Mono). Both approaches show consistently higher photometric error, since they do not optimize for stereo alignment. Note that the RGB-D tracker uses the ground truth depth as input.

	Photometric		Geometric	
	left	right	left	right
RGB Mono	0.0130	0.0574	0.2028	0.1994
RGB-D Mono	0.0123	0.0183	0.0031	0.0031
RGB Stereo (Ours)	0.0118	0.0116	0.0046	0.0046

Table 1: Tracking accuracy of our approach (RGB Stereo) compared to Thies et al. [2015] (RGB-D Mono) and Face2Face [2016] (RGB Mono). Our approach achieves low photometric and geometric errors for both views since we directly optimize for stereo alignment.

We evaluate the accuracy of our approach on ground truth data; see Fig. 14. As ground truth, we use high-quality stereo reconstructions obtained by Valgaerts et al. [2012]. To this end, we synthetically generate a high-quality binocular RGB-D stream from the reference data. Our approach achieves consistently low photometric and geometric errors. We also compare against the state-of-the-art face trackers of Thies et al. [2015] (RGB-D Mono) and Face2Face [Thies et al. 2016] (RGB Mono) on the same dataset. All three approaches are initialized using model-based RGB-(D) bundling of three (stereo) frames. The RGB and RGB-D trackers show consistently higher photometric errors for the right input stream, since they do not optimize for stereo alignment; see also Tab. 1. Given that Face2Face [Thies et al. 2016] only uses monocular color input, it suffers from depth ambiguity, which results in high geometric errors. Due to the wrong depth estimate, the re-projection to the right camera image does not correctly fit the input. The RGB-D based tracking approach of Thies et al. [2015] resolves this ambiguity and therefore obtains the highest depth accuracy. Note, however, that this approach has access to the ground truth depth data for the sake of this evaluation. Since the two cameras have slightly different response functions, the reconstructed model colors do not match the right image, leading to high photometric error. Only our model-based stereo tracker is able to obtain high-accuracy geometric and photometric alignment in both views. This is crucial for the creation of 3D stereo output for VR applications, as demonstrated in the VR applications. None of the two other approaches achieve this goal.

9 Limitations

Although FaceVR is able to facilitate a wide range of face appearance manipulations in VR, it is one of the early methods in a new field. As such, it is a first stepping stone and thus constrained by several limitations.

While our eye tracking solution provides great accuracy with little compute cost, it is specifically designed for the VR scenario. First, it is actor-specific, and we need to calibrate and train our classifier for each new person independently; this process takes only a few seconds, but it also makes the tracking solution less suitable compared to a general purpose eye tracker. Second, in the VR device, we track only one eye and infer the movement of the other eye. To correctly capture vergence and squinting one would need to add a second IR camera to the head mounted display. This is a straightforward modification; however, we wanted to keep our setup as simple as possible. Third, we assume that head rotation remains relatively constant with respect to its initialization. This always holds for tracking within an HMD since the IR camera is rigidly attached; it also works for facial reenactment, since both transfer and eye tracking is in model space. However, for general eye tracking, one would want to include the rigid head pose into the classification framework.

One important limitation of our approach is that we cannot modify the rigid head pose of the target videos. This would require a reconstruction of the background and the upper body of the actor, which we believe is an interesting research direction.

Our VR face tracking is based on the rigid head pose estimates and the unoccluded face regions. Unfortunately, the field of view of the IR camera attached to the inside of the device is not large enough to cover the entire interior face region. Thus, we cannot track most of the upper face except the eyeballs. Here, our method is complementary to the approach of Li et al. [2015]; they use additional sensor input from electronic strain measures to fill in this missing data. The resulting constraints could be easily included in our face tracking objective; note however, that their current tracking setup is different since the outside-in camera is rigidly attached to the HMD.

In the context of facial reenactment, we have similar limitations to Thies et al. [2015] and Face2Face [Thies et al. 2016]; i.e., we cannot handle occlusions in the target video such as those caused by microphones or waving hands. We believe that this could be addressed by computing an explicit foreground-face segmentation; the work by Saito et al. [2016] already shows promising results to specifically detect such cases.

10 Conclusion

In this work, we have presented *FaceVR*, a novel approach for real-time gaze-aware facial reenactment in the context of virtual reality. The key components of *FaceVR* are robust face reconstruction and tracking, data-driven eye tracking, and photo-realistic re-rendering of facial content on stereo displays. Therefore, we are able to show a variety of exciting applications, such as re-targeting of gaze directions in video chats, virtual removal of VR goggles in video streams, and most importantly, facial reenactment with gaze awareness in VR. We believe that this work is a stepping stone in this new field, demonstrating some of the possibilities of the upcoming virtual reality technology. In addition, we are convinced that this is not the end of the line, and we believe that there will be even more exciting future work targeting photo-realistic video editing in order to improve the VR experience, as well as many other related applications.

Acknowledgements

We thank Chen Cao, Kun Zhou, Volker Blanz, Thomas Vetter, and Oleg Alexander for providing their face datasets. The sparse landmark tracker was kindly provided by TrueVisionSolution. This research is funded by the German Research Foundation (DFG), grant GRK-1773 Heterogeneous Image Systems, the ERC Starting Grant 335545 CapReal, the Max Planck Center for Visual Computing and Communications (MPC-VCC), and a Google Tango grant.

References

- ALEXANDER, O., ROGERS, M., LAMBETH, W., CHIANG, M., AND DEBEVEC, P. 2009. The digital emily project: Photoreal facial modeling and animation. In *ACM SIGGRAPH 2009 Courses*, 12:1–12:15.
- BEELER, T., HAHN, F., BRADLEY, D., BICKEL, B., BEARDSLEY, P., GOTSMAN, C., SUMNER, R. W., AND GROSS, M. 2011. High-quality passive facial performance capture using anchor frames. In *ACM TOG*, vol. 30, 75:1–75:10.
- BLANZ, V., AND VETTER, T. 1999. A morphable model for the synthesis of 3d faces. In *ACM TOG*, 187–194.
- BLANZ, V., BASSO, C., POGGIO, T., AND VETTER, T. 2003. Re-animating faces in images and video. In *Proc. EUROGRAPHICS*, vol. 22, 641–650.
- BORSHUKOV, G., PIPONI, D., LARSEN, O., LEWIS, J. P., AND TEMPELAAR-LIETZ, C. 2003. Universal capture: image-based facial animation for "The Matrix Reloaded". In *SIGGRAPH Sketches*, 16:1–16:1.
- BOUAZIZ, S., WANG, Y., AND PAULY, M. 2013. Online modeling for realtime facial animation. *ACM TOG* 32, 4, 40:1–40:10.
- BREGLER, C., COVELL, M., AND SLANEY, M. 1997. Video rewrite: Driving visual speech with audio. In *ACM TOG*, 353–360.
- CAO, C., HOU, Q., AND ZHOU, K. 2014. Displaced dynamic expression regression for real-time facial tracking and animation. In *ACM TOG*, vol. 33, 43:1–43:10.
- CAO, C., WENG, Y., ZHOU, S., TONG, Y., AND ZHOU, K. 2014. Facewarehouse: A 3D facial expression database for visual computing. *IEEE TVCG* 20, 3, 413–425.
- CAO, C., BRADLEY, D., ZHOU, K., AND BEELER, T. 2015. Real-time high-fidelity facial performance capture. *ACM TOG* 34, 4, 46:1–46:9.
- CAO, C., WU, H., WENG, Y., SHAO, T., AND ZHOU, K. 2016. Real-time facial animation with image-based dynamic avatars. *ACM Trans. Graph.* 35, 4 (July).
- CRIMINISI, A., SHOTTON, J., BLAKE, A., AND TORR, P. H. 2003. Gaze manipulation for one-to-one teleconferencing. In *Proc. ICCV*.
- DALE, K., SUNKAVALLI, K., JOHNSON, M. K., VLASIC, D., MATUSIK, W., AND PFISTER, H. 2011. Video face replacement. In *ACM TOG*, vol. 30, 130:1–130:10.
- DEVITO, Z., MARA, M., ZOLLHÖFER, M., BERNSTEIN, G., RAGAN-KELLEY, J., THEOBALT, C., HANRAHAN, P., FISHER, M., AND NIESSNER, M. 2016. Opt: A domain specific language for non-linear least squares optimization in graphics and imaging. *arXiv preprint arXiv:1604.06525*.
- DING, C. H. Q., ZHOU, D., HE, X., AND ZHA, H. 2006. R1-pca: rotational invariant l1-norm principal component analysis for robust subspace factorization. In *ICML, ACM, W. W. Cohen and A. Moore, Eds., vol. 148 of ACM International Conference Proceeding Series*, 281–288.
- FYFFE, G., JONES, A., ALEXANDER, O., ICHIKARI, R., AND DEBEVEC, P. 2014. Driving high-resolution facial scans with video performance capture. *ACM Trans. Graph.* 34, 1 (Dec.), 8:1–8:14.
- GARRIDO, P., VALGAERTS, L., WU, C., AND THEOBALT, C. 2013. Reconstructing detailed dynamic face geometry from monocular video. In *ACM TOG*, vol. 32, 158:1–158:10.
- GARRIDO, P., VALGAERTS, L., REHMSSEN, O., THORMAEHLEN, T., PEREZ, P., AND THEOBALT, C. 2014. Automatic face reenactment. In *Proc. CVPR*.
- GARRIDO, P., VALGAERTS, L., SARMADI, H., STEINER, I., VARANASI, K., PEREZ, P., AND THEOBALT, C. 2015. Vdub - modifying face video of actors for plausible visual alignment to a dubbed audio track. In *CGF (Proc. EUROGRAPHICS)*.
- GARRIDO, P., ZOLLHÖFER, M., CASAS, D., VALGAERTS, L., VARANASI, K., PÉREZ, P., AND THEOBALT, C. 2016. Reconstruction of personalized 3d face rigs from monocular video. *ACM Transactions on Graphics (TOG)* 35, 3, 28.
- HSIEH, P.-L., MA, C., YU, J., AND LI, H. 2015. Unconstrained realtime facial performance capture. In *Proc. CVPR*.
- HUANG, H., CHAI, J., TONG, X., AND WU, H.-T. 2011. Leveraging motion capture and 3d scanning for high-fidelity facial performance acquisition. *ACM TOG* 30, 4 (July), 74:1–74:10.
- ICHIM, A. E., BOUAZIZ, S., AND PAULY, M. 2015. Dynamic 3d avatar creation from hand-held video input. *ACM TOG* 34, 4, 45:1–45:14.
- KAWAI, M., IWAO, T., MIMA, D., MAEJIMA, A., AND MORISHIMA, S. 2014. Data-driven speech animation synthesis fo-

- cusing on realistic inside of the mouth. *Journal of Information Processing* 22, 2, 401–409.
- KEMELMACHER-SHLIZERMAN, I., SANKAR, A., SHECHTMAN, E., AND SEITZ, S. M. 2010. Being John Malkovich. In *Proc. ECCV*, 341–353.
- KLEHM, O., ROUSSELLE, F., PAPAS, M., BRADLEY, D., HERY, C., BICKEL, B., JAROSZ, W., AND BEELE, T. 2015. Recent Advances in Facial Appearance Capture. *CGF (EUROGRAPHICS STAR Reports)*.
- KONONENKO, D., AND LEMPITSKY, V. 2015. Learning to look up: Realtime monocular gaze correction using machine learning. In *Proc. CVPR*, 4667–4675.
- KUSTER, C., POPA, T., BAZIN, J.-C., GOTSMAN, C., AND GROSS, M. 2012. Gaze correction for home video conferencing. *ACM Trans. Graph. (Proc. of ACM SIGGRAPH ASIA)* 31, 6, to appear.
- LABS, P., 2016. Pupil Labs. <https://pupil-labs.com/pupil/>. [Online; accessed 1-Sept-2016].
- LEWIS, J. P., ANJYO, K., RHEE, T., ZHANG, M., PIGHIN, F., AND DENG, Z. 2014. Practice and Theory of Blendshape Facial Models. In *Eurographics STARS*, 199–218.
- LI, K., XU, F., WANG, J., DAI, Q., AND LIU, Y. 2012. A data-driven approach for facial expression synthesis in video. In *Proc. CVPR*, 57–64.
- LI, H., YU, J., YE, Y., AND BREGLER, C. 2013. Realtime facial animation with on-the-fly correctives. In *ACM TOG*, vol. 32.
- LI, H., TRUTOIU, L., OLSZEWSKI, K., WEI, L., TRUTNA, T., HSIEH, P.-L., NICHOLLS, A., AND MA, C. 2015. Facial performance sensing head-mounted display. *ACM Transactions on Graphics (Proceedings SIGGRAPH 2015)* 34, 4 (July).
- OLSZEWSKI, K., LIM, J. J., SAITO, S., AND LI, H. 2016. High-fidelity facial and speech animation for vr hmds. *ACM Transactions on Graphics (Proceedings SIGGRAPH Asia 2016)* 35, 6 (December).
- OZUYSAL, M., CALONDER, M., LEPETIT, V., AND FUA, P. 2010. Fast keypoint recognition using random ferns. *IEEE Trans. Pattern Anal. Mach. Intell.* 32, 3 (Mar.), 448–461.
- PIGHIN, F., AND LEWIS, J. 2006. Performance-driven facial animation. In *ACM SIGGRAPH Courses*.
- PIGHIN, F., HECKER, J., LISCHINSKI, D., SZELISKI, R., AND SALESIN, D. 1998. Synthesizing realistic facial expressions from photographs. In *ACM TOG*, 75–84.
- RAMAMOORTHY, R., AND HANRAHAN, P. 2001. A signal-processing framework for inverse rendering. In *Proc. SIGGRAPH*, ACM, 117–128.
- SAITO, S., LI, T., AND LI, H. 2016. Real-time facial segmentation and performance capture from rgb input. In *Proceedings of the European Conference on Computer Vision (ECCV)*.
- SARAGIH, J. M., LUCEY, S., AND COHN, J. F. 2011. Deformable model fitting by regularized landmark mean-shift. *IJCV* 91, 2, 200–215.
- SHI, F., WU, H.-T., TONG, X., AND CHAI, J. 2014. Automatic acquisition of high-fidelity facial performances using monocular videos. In *ACM TOG*, vol. 33.
- SUGANO, Y., MATSUSHITA, Y., AND SATO, Y. 2014. Learning-by-synthesis for appearance-based 3d gaze estimation. In *Proc. CVPR*, 1821–1828.
- SUWAJANAKORN, S., KEMELMACHER-SHLIZERMAN, I., AND SEITZ, S. M. 2014. Total moving face reconstruction. In *Proc. ECCV*, 796–812.
- SUWAJANAKORN, S., SEITZ, S. M., AND KEMELMACHER-SHLIZERMAN, I. 2015. What makes tom hanks look like tom hanks. In *Proc. ICCV*.
- TAYLOR, S. L., THEOBALD, B., AND MATTHEWS, I. A. 2015. A mouth full of words: Visually consistent acoustic redubbing. In *ICASSP*, IEEE, 4904–4908.
- TENA, J. R., DE LA TORRE, F., AND MATTHEWS, I. 2011. Interactive region-based linear 3d face models. *ACM TOG* 30, 4, 76:1–76:10.
- THIES, J., ZOLLHÖFER, M., NIESSNER, M., VALGAERTS, L., STAMMINGER, M., AND THEOBALT, C. 2015. Real-time expression transfer for facial reenactment. *ACM TOG* 34, 6, 183:1–183:14.
- THIES, J., ZOLLHÖFER, M., STAMMINGER, M., THEOBALT, C., AND NIESSNER, M. 2016. Face2Face: Real-time Face Capture and Reenactment of RGB Videos. In *Proc. Computer Vision and Pattern Recognition (CVPR)*, IEEE.
- VALGAERTS, L., WU, C., BRUHN, A., SEIDEL, H.-P., AND THEOBALT, C. 2012. Lightweight binocular facial performance capture under uncontrolled lighting. In *ACM TOG*, vol. 31, 187:1–187:11.
- VLASIC, D., BRAND, M., PFISTER, H., AND POPOVIC, J. 2005. Face transfer with multilinear models. In *ACM TOG*, vol. 24, 426–433.
- WANG, C., SHI, F., XIA, S., AND CHAI, J. 2016. Realtime 3d eye gaze animation using a single rgb camera. *ACM Trans. Graph.* 35, 4 (July).
- WEISE, T., LI, H., GOOL, L. J. V., AND PAULY, M. 2009. Face/Off: live facial puppetry. In *Proc. SCA*, 7–16.
- WEISE, T., BOUAZIZ, S., LI, H., AND PAULY, M. 2011. Realtime performance-based facial animation. In *ACM TOG*, vol. 30, 77:1–77:10.
- WILLIAMS, L. 1990. Performance-driven facial animation. In *Proc. SIGGRAPH*, 235–242.
- WU, C., ZOLLHÖFER, M., NIESSNER, M., STAMMINGER, M., IZADI, S., AND THEOBALT, C. 2014. Real-time shading-based refinement for consumer depth cameras. *ACM Transactions on Graphics (TOG)* 33, 6.
- ZHANG, L., SNAVELY, N., CURLESS, B., AND SEITZ, S. M. 2004. Spacetime faces: high resolution capture for modeling and animation. In *ACM TOG*, vol. 23, 548–558.
- ZHANG, X., SUGANO, Y., FRITZ, M., AND BULLING, A. 2015. Appearance-based gaze estimation in the wild. In *CVPR*, 4511–4520.
- ZOLLHÖFER, M., NIESSNER, M., IZADI, S., REHMANN, C., ZACH, C., FISHER, M., WU, C., FITZGIBBON, A., LOOP, C., THEOBALT, C., AND STAMMINGER, M. 2014. Real-time non-rigid reconstruction using an rgb-d camera. In *ACM TOG*, vol. 33.
- ZOLLHÖFER, M., DAI, A., INNMANN, M., WU, C., STAMMINGER, M., THEOBALT, C., AND NIESSNER, M. 2015. Shading-based refinement on volumetric signed distance functions. *ACM Transactions on Graphics (TOG)* 34, 4.